OPEN ACCESS Freely available online

IJCMB
International Journal of Clinical Medicine and Bioengineering

ISSN 2737-534X
Volume 6
Issue 1
International Journal of Clinical Medicine and Bioengineering

Article

Optimizing Diopside for Bone Repair: Structural, Mechanical, and Biological Effects of Ce/Co Co-Substitution

Hsiu-Wen Yang [1], Yun-Han Su [1], Yu-Sheng Tseng [1], Dorian Amir Henry Hanaor [2], Wen-Fan Chen [1,*]

[1] Institute of Medical Science and Technology, National Sun Yat-sen University, Kaohsiung 80424, Taiwan; wendy20011261022@gmail.com (H.-W.Y.); vicky0122@mem.nsysu.edu.tw (Y.-H.S.); johnson760515@gmail.com (Y.-S.T.)

[2] Faculty of Science and Engineering, Southern Cross University, East Lismore, NSW, 2480, Australia; dorianhanaor@gmail.com (D.A.H.H.)

* Correspondence: sallychen@imst.nsysu.edu.tw

Received: Nov 27, 2025; **Revised:** Feb 04, 2026; **Accepted:** Mar 23, 2026; **Published:** Mar 30, 2026

Abstract: We examined the influence of simultaneous cerium (Ce) and cobalt (Co) substitution in diopside ($CaMgSi_2O_6$) on its structural, mechanical, and biological behavior. Moderate incorporation levels (0.25–0.50 mol of Ce/0.25–0.50 mol of Co) produced the most balanced performance. At the Ce 0.50 mol/Co 0.50 mol composition, the material achieved the highest hardness (174.8 Hv), a remarkable enhancement compared with pure diopside (14.9 Hv), which is attributed to improved microstructural densification. In contrast, high co-substitution levels (≥ 0.75/0.75 mol) caused lattice distortion, increased porosity, and reduced mechanical stability. Bioactivity tests showed that the Ce 0.25 mol/Co 0.25 mol composition presented hydroxyapatite formation in simulated body fluid, while excessive co-substitution suppressed Ca, Si, and P participation and limited hydroapatite nucleation. Cell assays revealed a clear decrease in viability with increasing Co content, indicating that Co release is the primary factor affecting cytocompatibility and mineralization ability. Through low-to-moderate Ce/Co substitution, mechanical strength enhances while maintaining acceptable mineralization capability, whereas high substitution compromises performance. The Ce 0.25–0.50 mol/Co 0.25–0.50 mol compositions exhibited optimal performance, while further reduction of Co content effectively lowered cytotoxicity.

Keywords: $CaMgSi_2O_6$, Cerium, Cobalt, Co-substitution, Bioceramic

1. Introduction

The rapid progression of global population aging has been a pressing public health challenge. By 2050, the number of individuals aged 65 and older is projected to more than double, reaching 1.5 billion and accounting for 16% of the global population [1]. This demographic shift is closely associated with an increased prevalence of musculoskeletal disorders, which impose a substantial burden on healthcare systems worldwide. Osteoarthritis, in particular, represents a leading cause of articular cartilage degeneration and pathological deterioration, with its incidence rising sharply among populations over 50 years of age. In addition, bone defects resulting from trauma, infection, or tumor resection are frequently encountered in clinical practice [2]. Collectively, these conditions underscore the urgent need for advanced biomaterials capable of supporting effective bone repair and regeneration.

Traditional grafting approaches, including autografts, allografts, and xenografts, have long been used for bone defect repair. However, their limitations, such as donor site morbidity, limited availability, risk of disease transmission, and inconsistent quality, have spurred growing interest in the development of synthetic bone substitutes. These substitutes have consistent quality, improved safety, and enhanced biological performance, and are fabricated from materials with favorable biocompatibility, corrosion resistance, and mechanical robustness, including titanium alloys [3], biodegradable polymers [4] acrylic bone cements, and high-density polyethylene. Despite these advantages, synthetic materials present drawbacks. Metallic implants might release and diffuse ions into surrounding tissues, potentially inducing inflammatory responses, while polymer-based substitutes can leach cytotoxic residual monomers due to incomplete polymerization. In contrast, ceramic materials demonstrate superior chemical stability and biocompatibility in vivo, enabling direct chemical bonding with host tissues and even contributing to new bone formation. This makes ceramics promising candidates for hard-tissue replacement. Among them, calcium phosphate ceramics, particularly tricalcium phosphate and silicate-based bioceramicsm have been extensively researched owing to their excellent osteoconductivity and intrinsic bioactivity.

To further enhance the regenerative potential of these materials, growth factor–based methods have been introduced. However, the methods raise safety concerns and unpredictable immunological responses [5]. In contrast, bioinorganic ions promote osteogenesis through physiologically aligned and inherently safer mechanisms. Bioinorganic elements such as silicon, magnesium, strontium, and zinc act as cofactors for enzymes, coenzymes, and metalloenzymes, offering advantages over growth factors,

including lower cost, extended storage stability, and reduced biological risk [6]. The biological roles and mechanisms of these bioinorganic ions, in promoting osteogenesis and angiogenesis, are summarized in Table 1.

Table 1. Biological effects of exogenous ion supplementation on bone-related cellular responses.

Ion	Primary biological effect(s)	Mechanism of action	Cell type/ion dosage	Reference
Mg^{2+}	Osteogenesis; Angiogenesis; Neurogenic stimulation	In undifferentiated and differentiated human bone marrow, derived mesenchymal stem cells, Mg^{2+} stimulates the production of regulatory factors that indirectly enhance VEGF secretion.	Mouse pre-osteoblasts, 50–150 ppm	[7]
		Mg^{2+} also enters neurons and promotes calcitonin gene-related peptide release, which subsequently upregulates osteogenic gene expression in periosteal stem cells.	Human bone marrow stem cells, 5–10 mM	[8,9]
Sr^{2+}	Osteogenesis	• Sr^{2+} enhances osteoblast activity while suppressing osteoclast-mediated resorption. • It activates Ca-sensing receptors and downstream signaling, increases anti-resorptive molecule production, reduces expression of osteoclast-activating membrane proteins, and induces osteoclast apoptosis.	Rat bone marrow (derived stem cells); Primary osteoblasts; <1 mM	[10,11]
Si^{4+}	Osteogenesis; Angiogenesis	• In co-culture with human dermal fibroblasts, Si^{4+} promotes angiogenesis by regulating nitric oxide synthase and enhancing VEGF expression at low concentrations. • Although its mechanism in osteogenesis is not fully defined, elevated Si^{4+} levels are known to play critical roles during mineralization.	Human osteoblasts (MG-63), 10–20 μM; Human mesenchymal stem cells, <100 μg/mL	[12,13]
Zn^{2+}	Osteogenesis	• Zn^{2+} participates in the expression, catalytic activity, and regulation of alkaline phosphatase, thereby contributing to osteogenesis and mineralization. • It also inhibits osteoclast-mediated bone resorption.	Mouse pre-osteoblasts, 10^{-5} M; Rat bone marrow (derived stem cells), 10^{-5} M	[14-16]
Li^{+}	Osteogenesis	Li^{+} suppresses GSK-3β activity and serves as an activator of the Wnt/β-catenin pathway, thereby enhancing osteogenesis and accelerating fracture healing.	Mouse model; 0.02 M administered via daily drinking water	[17]
Co^{2+}	Angiogenesis	Co^{2+} induces a hypoxia-mimicking response by stabilizing hypoxia-inducible factor (HIF), leading to upregulation of genes associated with neovascularization and angiogenesis.	Human bone marrow (derived mesenchymal stem cells), 100 mM or 20 mg/L	[18–20]

In addition to the introduction of new materials, diverse strategies have been developed to optimize the mechanical and biological performance of bone substitutes, including the incorporation of natural [21] or synthetic [22] biopolymers, surface-coating treatments [23], and elemental doping or substitution [24]. Among these, ion doping is considered particularly promising, as it reinforces mechanical strength and biological functionality at the same time. In the method, doped ions have fostered mineralization, increased ceramic densification [25], and modulated grain size and morphology, which are closely associated with bioactivity [26]. Moreover, the release kinetics of these ions substantially influence the material's overall biological response [27].

Among the ions, Ce^{3+} possesses electronegativity and ionic radii similar to Ca^{2+} (Ce^{3+}: 1.06 and 0.107 nm; Ca^{2+}: 1.01 and 0.100 nm [28,29]), while Co^{2+} exhibits ionic characteristics analogous to Mg^{2+} [Co^{2+}: 1.88 and 0.065 nm (high spin) / 0.0745 nm (low spin); Mg^{2+}: 1.31 and 0.072 nm] [30]. These similarities enable the substitutions of Ce^{3+} to Ca^{2+} and Co^{2+} to Mg^{2+} in the diopside lattice, altering its chemical composition and structural configuration. Importantly, Ce^{3+} is known to regulate bone remodeling, enhance metabolic activity, and exhibit antibacterial properties [31–35], while Co^{2+} is known to induce hypoxic responses, stimulate angiogenesis, and promote osteogenesis [36,37]. On ths bases of the previous research results, we investigate the co-substitution of cobalt (Co) and cerium (Ce) ions into diopside ($CaMgSi_2O_6$) to develop bioactive ceramic materials with enhanced functionality in this study.

2. Materials and Methods

2.1.Sample Fabrication

1 mol of CaMgSi2O6 powders were synthesized using a precipitation method. Calcium chloride ($CaCl_2$, 95%, Fisher Scientific, the United Kingdom), magnesium chloride hexahydrate ($MgCl_2 \cdot 6H_2O$, EMSURE, Germany), and tetraethyl silicate (TEOS, Seedchem, Australia) were dissolved in 95% ethanol and stirred for 2 hours to obtain a homogeneous precursor solution. Ammonium hydroxide (28%, Nihon shiyaku reagent, Japan) was then added, and the mixture was heated at 80°C for ethanol evaporation and precipitation. After 24 hours of continuous stirring, the precipitate was dried at 80°C for 24 hours, ground into fine powder, and calcined at 600°C for 3 hours to remove impurities and avoid diopside crystallization. The crystallization occurs at 850–950°C [38,39]. The resulting powders were pressed into 13 (diameter) × 1.8 (thickness) mm pellets 9 at 75 MPa for 30 seconds and underwent a two-stage sintering process: removing moisture at 250°C for 2 hours and desifying by 1000°C for 4 hours.

Ce/Co co-substituted CaMgSi2O6 nanoparticles are prepared in the following procedure. $CaCl_2$, $MgCl_2 \cdot 6H_2O$, TEOS, and varying ratios of cerium chloride heptahydrate ($CeCl_3 \cdot 7H_2O$, 99%, Alfa Aesar, USA), anhydrous cobalt chloride ($CoCl_2$, 97%, Alfa Aesar, USA) were mixed in ethanol, stirred for 2 hours, and precipitated with NH_4OH at 80°C. Subsequently, the participate was dried, ground, calcinated, and sintered to obtain the pure diopside powders. In this study, Ce^{3+} substitutes for Ca^{2+} and Co^{2+} for Mg^{2+}, with the level ranging from 0–100 mol% (Table 2). The overall synthesis process is illustrated in Fig. 1

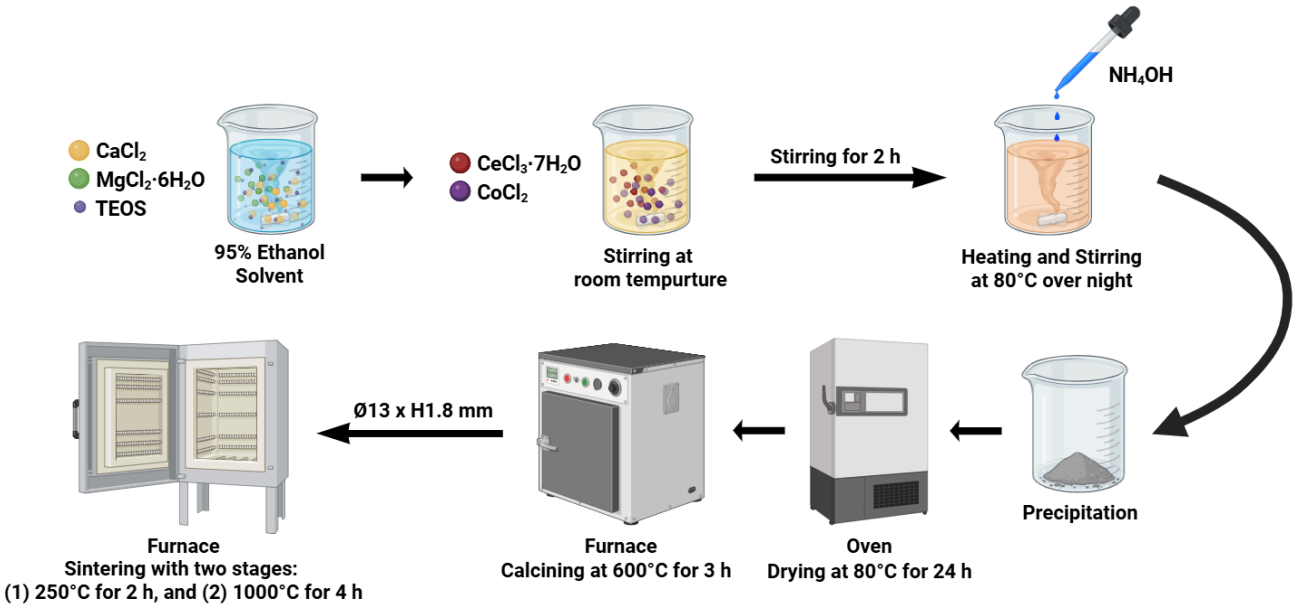

Fig. 1. The ssynthesis procedure of Ce/Co-substituted CaMgSi2O6 bioceramics via the precipitation method.

Table 2. Molar ratios of Ce^{3+} and Co^{2+} substituting for Ca^{2+} and Mg^{2+} in $CaMgSi_2O_6$ ($Ca_{(1-y)}Mg_{(1-x)}Co_xCe_ySi_2O_{6)}$.

Sample	$CaCl_2$ (mole)	$MgCl_2{\cdot}6H_2O$ (mole)	TEOS (mole)	$CeCl_3{\cdot}7H_2O$ (mole)	$CoCl_2$ (mole)
1	0.01	0.01	0.02	-	-
2	0.0075	0.0075	0.02	0.0025	0.0025
3	0.005	0.005	0.02	0.005	0.005
4	0.0025	0.0025	0.02	0.0075	0.0075
5	0	0	0.02	0.01	0.01

2.2. Characterization

The crystal structure and phase composition were characterized using X-ray diffractometry (D2 Phaser, Bruker, USA) with Cu-Kα radiation (λ = 1.5418 Å) over a 2θ range of 10°–70° at 30 kV and 10 mA, with a scan rate of 0.01°/s. Phase identification was performed using Match! software (Crystal Impact, Germany). Surface morphology and microstructural features were examined by environmental scanning electron microscopy (Environmental Scanning Electron Microscope, FEI Quanta 200, Philips, Netherlands). Due to the low conductivity of the ceramic materials, samples were sputter-coated with gold to prevent charging artifacts during imaging. Hardness was measured using a Vickers hardness tester (FM-810, Future-Tech, Japan) under a load of 200 gram-force for 10 seconds.

2.3. In Vitro Biodegradation and Apatite Formation Analysis

To evaluate the in vitro bioactivity and degradation behavior, pH variation, weight loss, and ion release were analyzed. Simulated body fluid (SBF) was prepared following Kokubo *et al*'s method [40]. Samples were immersed in SBF at 37°C, with the required solution volume calculated using Equation (1).

$$Vs = \frac{S_A}{10}, \quad (1)$$

where Vs is the SBF volume (mL), and S_A is the sample surface area (mm^2). The pH of the immersion media was measured on days 7, 14, 21, and 28 using a pH meter (pH 510, Eutech, Singapore) to assess the influence of dissolution and ion exchange on the solution environment. Weight loss (W_L %) after immersion was calculated using Equation (2).

$$W_L = \frac{(W_0 - W_F)}{W_0} \times 100\ (\%), \quad (2)$$

where W_0 and W_F denote the initial and final sample weights, respectively. For ion release analysis, SBF solutions collected at days 14 and 28 were examined by inductively coupled plasma-mass spectrometry (Inductively Coupled Plasma Mass Spectrometry, ELEMENT X, Thermo Fisher Scientific, USA) to quantify Ca, Mg, Si, Ce, Co, and P concentrations, thereby assessing dissolution and re-mineralization behavior under physiological conditions.

2.4. Cell Viability Assay

The 3-(4,5-dimethylthiazol-2-yl)-2,5-diphenyl tetrazolium bromide (MTT) assay (98%, Alfa Aesar, USA) was performed using liquid extracts of the bioceramic samples. Dulbecco's Modified Eagle Medium (DMEM) powder medium (GIBCO, USA) was prepared with deionized (DI) water, supplemented with 3.7 g/L $NaHCO_3$, 10% fetal bovine serum (FBS), and 0.5% penicillin-streptomycin (Sigma-Aldrich, USA). The medium was sterilized through a 0.22 μm filter and stored at 4°C. MTT stock solution (5 mg/mL) was prepared in PBS and filtered through a 0.22 μm membrane before use. The assay was prepared through extract preparation, sample exposure, and MTT reaction.

- Day 1: Extract preparation
  Mouse mesenchymal stem cells (D1) were seeded at 0.2×10^4 cells/well in 96-well plates and incubated at 37°C with 5% CO_2 for 24 hours. Sample extracts were prepared at 0.2 g/mL. Sodium dodecyl sulfate (0.2 mg/mL) was used as the positive control and alumina (0.2 g/mL) as the negative control. All materials were immersed in DMEM and incubated at 37°C for 24 hours.
- Day 2: Sample testing
  After extraction, all solutions were filtered, and 100 μL of each extract was used to replace the culture medium in each well. Cells were incubated for another 24 hours.
- Day 3: MTT reaction

MTT solution (100 μL/well) was added and incubated for 2 hours. Formazan crystals were dissolved with 100 μL/well of dimethyl sulfoxide and absorbance was measured at 570 nm. Cell viability was calculated as

$$\text{Cell viability (\%)} = \frac{OD_S}{OD_C} \times 100\ (\%) \quad (3)$$

where OD_S and ODc denote the absorbance of the sample and cell-only control groups, respectively. Data are presented as mean ± standard deviation. Statistical significance p was lower than 0.05.

2.5. In-vitro Bone Mineralization

Cell mineralization was assessed using Alizarin Red S (ARS) staining. The osteogenic induction medium (OIM) was prepared using DMEM supplemented with 3.7 g/L $NaHCO_3$, 10% FBS, 0.5% penicillin-streptomycin, L-ascorbic acid, β-glycerol phosphate disodium salt, and dexamethasone (Sigma-Aldrich, USA). ARS staining solution was prepared by dissolving ARS sodium salt (Alfa Aesar, USA) in DI water to a final concentration of 2% and adjusting the pH to 4.2.

- Day 1: Cell seeding
  D1 cells were seeded in 48-well plates at 2.5×10^4 cells/well and cultured in DMEM at 37°C and 5% CO_2 for 2 days.
- Day 2: Extract preparation
  Samples were immersed in OIM at 0.0125 g/mL and incubated at 37°C for 24 h.
- Day 3: Extract treatment
  Extracts were filtered, and 250 μL of extract was used to replace the culture medium in each well. Cells were cultured in the extracts for 4 days under standard incubation conditions.
- Day 7: ARS staining
  The culture medium was removed, and cells were washed with PBS. A volume of 200 μL/well of 4% paraformaldehyde was added for 10 min to fix the cells. After rinsing with ultrapure water, 200 μL/well of ARS solution was applied for staining. The calcium-bound dye was then eluted using 10% acetic acid, and absorbance was measured at 570 nm using an Enzyme-Linked Immunosorbent Assay.

3. Results

The X-ray diffraction (XRD) patterns of diopside co-substituted with various Ce/Co ratios are shown in Fig. 2. The main phases in all samples were $CaMgSi_2O_6$ (the Inorganic Crystal Structure Database (ICSD) 52359) and CeO_2 (ICSD 28753), while no Co-related crystalline phases were observed in Fig. 2(a). According to previous studies, this is likely due to the incorporation of Co ions into CeO_2 lattice sites rather than forming separate Co-containing phases [41-43]. The unchanged CeO_2 diffraction profile shows the formation of a Co-Ce-O solid solution [41]. When the Ce/Co substitution reached 0.50 mol/0.50 mol, the diffraction peaks shifted slightly toward higher angles with increasing dopant content. This shift is attributed to the smaller ionic radius of Co^{2+} relative to Ce^{4+}, leading to a reduced unit-cell volume when Co^{2+} occupies Ce^{4+} lattice positions [44], confirming the solid solution incorporation of Co^{2+}. Figure 2(b) shows the XRD results after SBF immersion.

In addition to $CaMgSi_2O_6$ and CeO_2, new peaks corresponding to hydroxyapatite (HAp) ($Ca_5(PO_4)_3OH$, ICSD 34457) appeared, indicating apatite deposition on the sample surface. The Ce 0.25 mol/Co 0.25 mol group exhibited the strongest HAp signals, suggesting optimal remineralization capability at this substitution level. As the Ce/Co ratio increased, the $CaMgSi_2O_6$ peak intensity decreased, and in the high-substitution group (Ce 1.00 mol/Co 1.00 mol), HAp signals were hardly detectable, demonstrating that excessive ion substitution inhibits apatite formation. These observations indicate that low-level Ce/Co co-substitution preserves phase stability while enhancing surface bioactivity and promoting biomineralization in SBF.

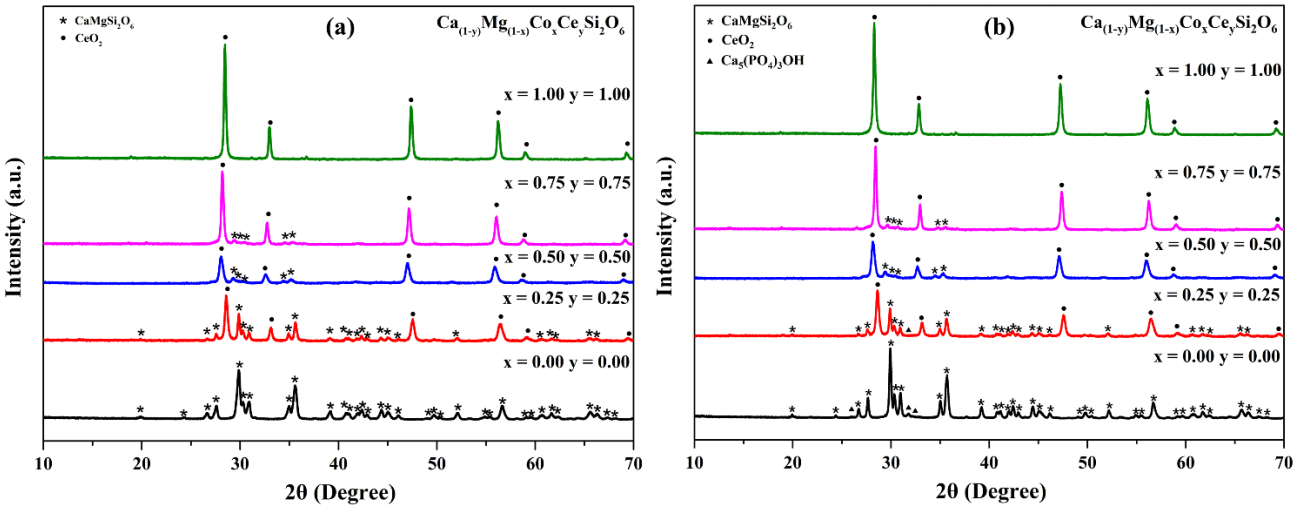

Fig. 2. XRD patterns of pure and Ce/Co co-substituted diopside samples: **(a)** after sintering at 1000°C for 4 h; **(b)** after immersion in SBF.

Figure 3 presents the Scanning Electron Microscopy (SEM) microstructures of pure and Ce/Co co-substituted samples before and after 28 days of immersion in SBF. Before immersion, the sample with Ce 0.50 mol/Co 0.50 mol exhibited the densest surface structure. As the Ce/Co substitution level increased beyond this, the surface became progressively more porous, with porosity increasing alongside the dopant concentration. For the Ce/Co co-substituted samples, no spherical HAp precipitates were observed when the substitution levels were high. The absence of HAp formation is attributed to the replacement of Ca and Mg ions in the diopside lattice by Ce and Co, which reduces the availability of Ca/Mg and alters the overall crystal structure, thereby hindering the nucleation and growth of HAp. In contrast, the Ce 0.25 mol/Co 0.25 mol sample exhibited scattered HAp deposits, although less pronounced than those observed on pure diopside. Although HAp formation was lower than in the pure sample, low-level Ce/Co substitution maintained the material's intrinsic mineralization bioactivity. This is consistent with the XRD results, confirming that excessive Ce/Co incorporation suppresses bioactive surface reactions in SBF.

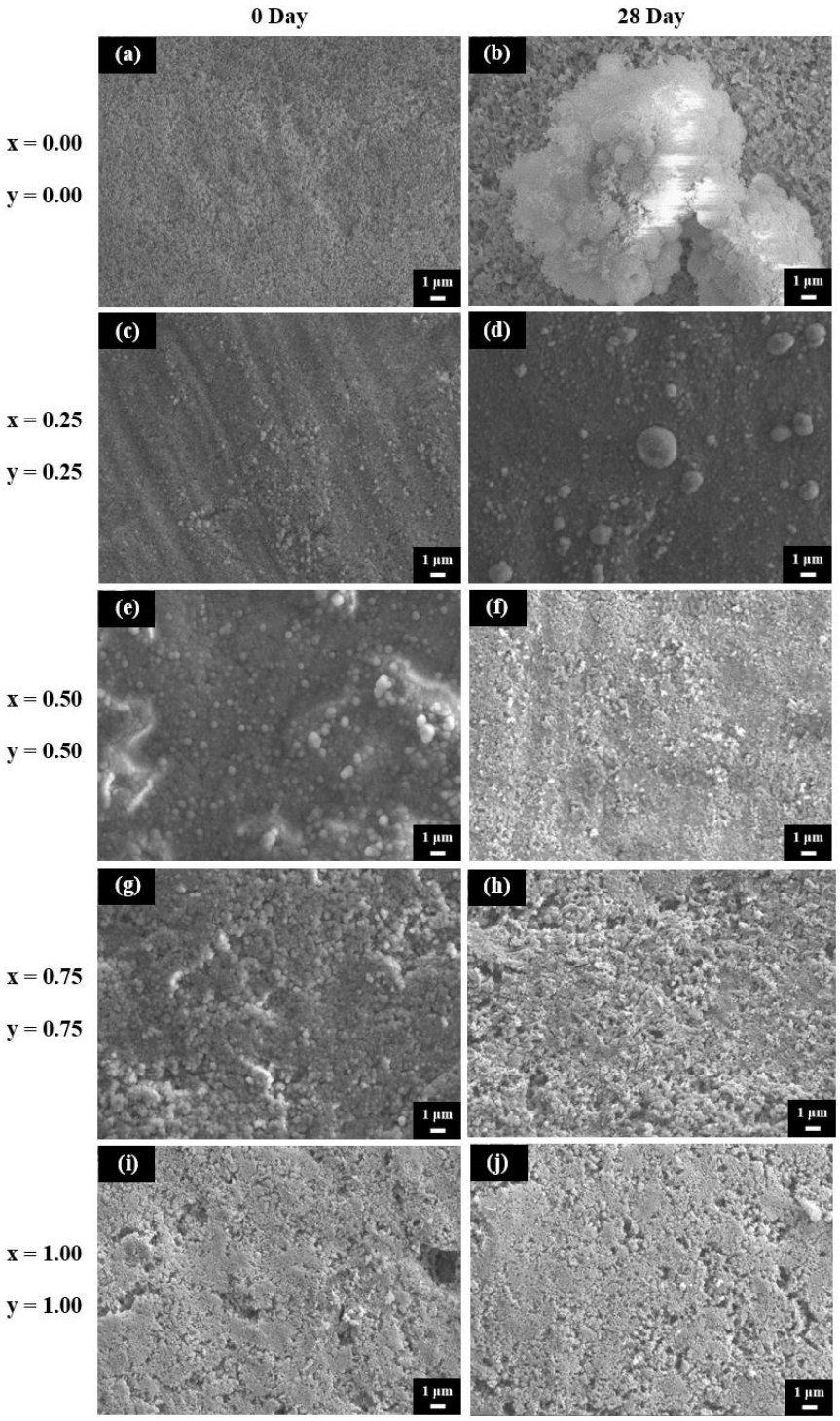

Fig. 3. Comparison of the microstructural features of diopside samples with varying Ce/Co co-substituted levels (5000X).

The Vickers hardness values of the samples are presented in Fig. 4, from five repeated measurements to ensure measurement accuracy and reproducibility. The pure specimen (x = 0.00, y = 0.00) exhibited the lowest hardness of 14.9 Hv due to its higher porosity and insufficient structural integrity. As the Ce and Co substitution levels increased to Ce 0.25 mol/Co 0.25 mol, the hardness improved to 93.8 Hv, and increased to the maximum of 174.8 Hv at Ce 0.50 mol/Co 0.50 mol. The measured range aligns with typical hardness values of densified diopside and other bioactive silicate ceramics, supporting the plausibility of the observed >10-fold enhancement in systems undergoing substantial porosity reduction and improved microstructural packing. This increase is attributed to the development of a denser, more interconnected microstructure, consistent with the SEM observations presented in Fig. 3.

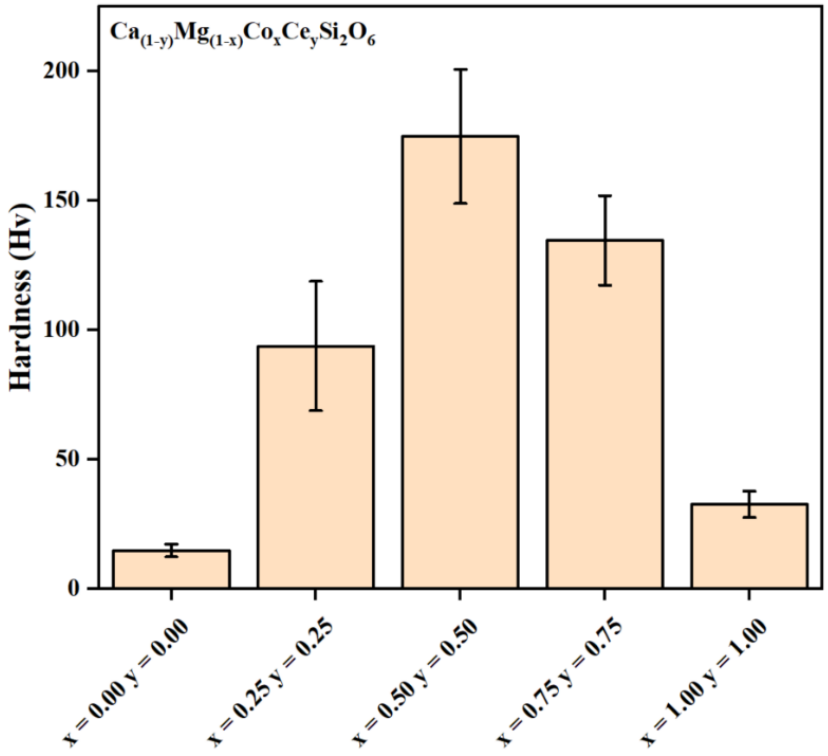

Fig. 4. Vickers hardness of diopside samples with varying Ce/Co co-substituted levels (n = 5).

When the co-substitution level was increased to Ce 0.75 mol/Co 0.75 mol and Ce 1.00 mol/Co 1.00 mol, the hardness decreased to around 134.6 and 32.8 Hv, respectively. This decrease is caused by excessive dopant incorporation, which promotes secondary phase formation, increases lattice distortion, and leads to microstructural heterogeneity. These effects weaken grain boundary cohesion, and SEM confirms the resulting increase in porosity and localized defects. The difference between the pure and substituted samples highlights the influence of Ce/Co incorporation on densification behavior. Overall, the results demonstrate that moderate Ce/Co co-substituted levels strengthen diopside-based bioceramics by optimizing microstructural densification, whereas excessive co-substitution induces structural imbalance and deteriorates mechanical performance.

The pH variations of pure diopside and Ce/Co co-substituted samples after immersion in SBF for 7, 14, 21, and 28 days are shown in Fig. 5(a). All samples exhibited a rapid increase in pH during the first 7 days. For the Co 0.50 mol/Ce 0.50 mol, Co 0.75 mol/Ce 0.75 mol, and Co 1.00 mol/Ce 1.00 mol samples, pH approached equilibrium after 14 days, whereas the Co 0.25 mol/Ce 0.25 mol group showed only a slight increase in pH during the same period. Compared with pure diopside, all co-substituted samples displayed smaller pH fluctuations, suggesting that the ion-exchange reactions between H^+/H_3O^+ and Ca^{2+}/Mg^{2+} were less pronounced in the co-substituted samples. This indicates that the dissolution and precipitation rates are rapidly balanced, resulting in a stable solution. The reduced pH variation observed in co-substituted samples may be advantageous for potential implant applications, as it minimizes drastic changes in the surrounding physiological environment, providing a favorable and biocompatible surface for tissue interaction.

The weight loss of Ce/Co co-substituted diopside samples after immersion in SBF for 7, 14, 21, and 28 days is shown in Fig. 5(b). Among the low-to-moderate substitution groups (Co 0.25 mol/Ce 0.25 mol, Co 0.50 mol/Ce 0.50 mol, and Co 0.75 mol/Ce 0.75 mol), the weight loss trends were generally similar, exhibiting slight weight gain after 28 days due to surface HAp deposition. In particular, the Co 0.50 mol/Ce 0.50 mol sample, which displayed the densest microstructure and highest hardness, showed the slowest degradation and weight gain, indicating that its structural compactness effectively retarded dissolution. In contrast, the pure diopside exhibited rapid weight loss, attributable to its lower hardness and higher porosity, which facilitated faster degradation. The Co 1.00 mol/Ce 1.00 mol sample experienced significant weight reduction after 28 days, likely due to complete substitution of Ca and Mg ions, lattice alteration, and accelerated ion release. This suggests that the dissolution rate of cations in the highly substituted sample exceeded the re-adsorption rate of ions from SBF onto the sample surface. Overall, the weight loss and degradation behavior were closely correlated with both sample microstructure and HAp formation capability. Denser samples degraded more slowly while promoting HAp deposition, whereas porous, softer samples degraded faster with less effective mineralization.

The release of Co ions from Ce/Co co-substituted samples increased with higher substitution levels (Fig. 5(c)). Samples with larger Co content released more Co into the SBF over the immersion period. This indicates that the ion release is directly related to the dopant concentration and reflects the structural incorporation of Co within the diopside lattice. As shown in Fig. 5(d), Ca ion release increased after 14 days for all groups except the Ce 0.25 mol/Co 0.25 mol sample, including the pure diopside control. Compared with pure diopside, all co-substituted samples exhibited slower Ca dissolution after 28 days of immersion, with the Ce 0.25 mol/Co 0.25 mol group showing the slowest release. This reduced Ca depletion indicates enhanced structural stability and suggests that the Ce 0.25 mol/Co 0.25 mol composition is particularly favorable for implant applications.

As shown in Fig. 5(e), Mg ion release remained relatively stable across most groups, with no substantial dissolution or re-adsorption observed, except for the pure diopside and the Ce 0.25 mol/Co 0.25 mol samples. This suggests that Mg ions played a minimal role in governing the pH variation during immersion. Further, the overall Mg release decreased with increasing Ce/Co substitution levels, indicating that higher dopant concentrations may suppress Mg mobility within the diopside lattice, thereby reducing its release into the SBF.

All samples, including pure diopside and the Ce/Co co-substituted groups, exhibited a continuous release of Si ions throughout the immersion period (Fig. 5(f)). This sustained release facilitates the formation of surface Si-OH groups, which promote the nucleation of HAp. The results show that increasing levels of Ce and Co substitution progressively suppressed Si ion release, indicating that dopant incorporation into the diopside lattice hinders Si mobility and thereby reduces its dissolution into the SBF. As shown in Fig. 5(g), the P ion concentration in SBF decreased over time for the pure diopside and the Ce 0.25 mol/Co 0.25 mol samples, indicating active phosphate uptake associated with HAp formation, consistent with the surface observations in Fig. 3. In contrast, the other co-substituted groups displayed a similar trend of minimal or no decrease in P ion concentration, suggesting that higher levels of Ce/Co co-substitution hinder phosphate adsorption and consequently suppress HAp deposition. Notably, Ce ions were not detected, most likely because their concentration released into the SBF solution was below the detection limit.

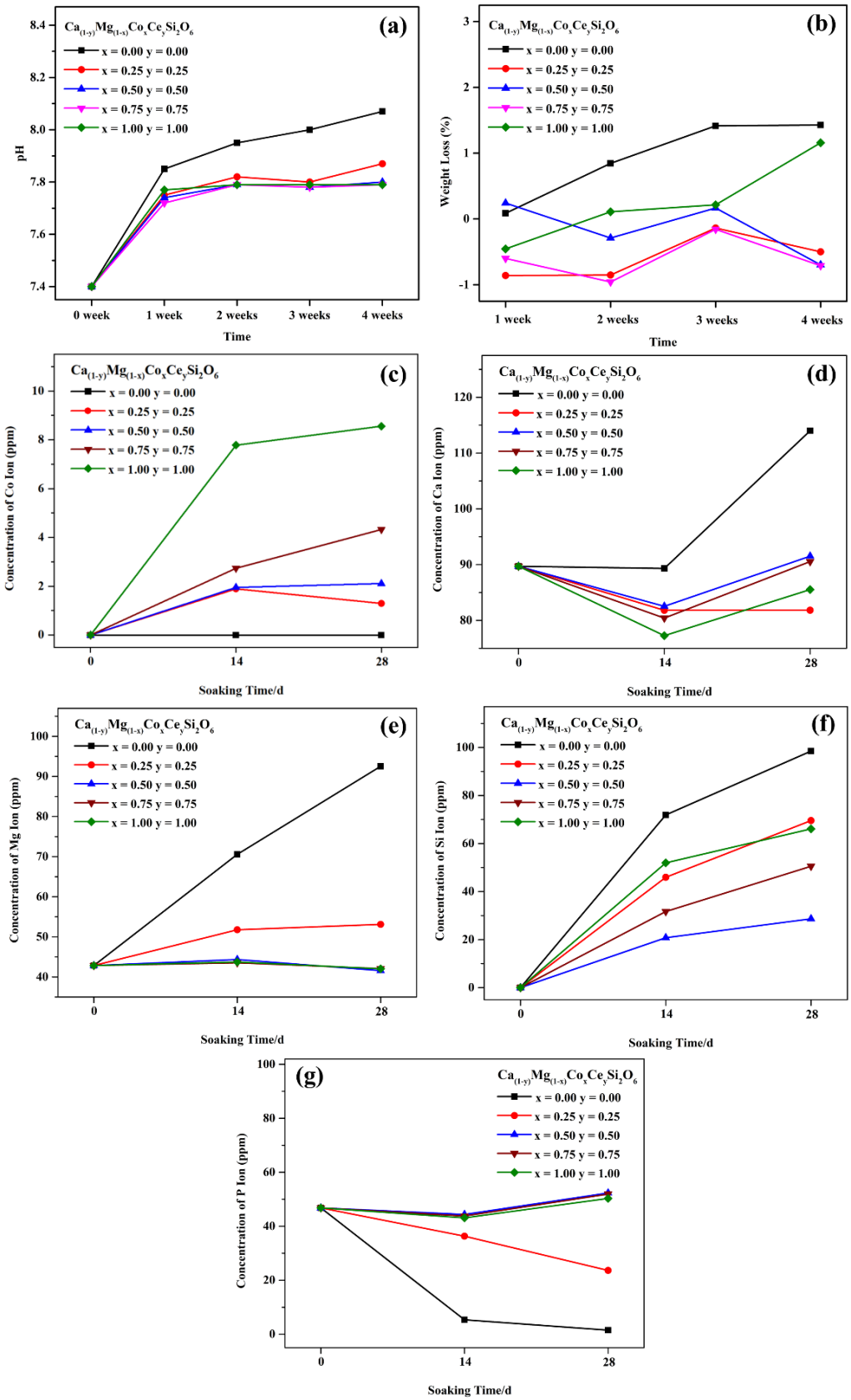

Fig. 5. (a) Variations in pH; **(b)** weight loss of Ce/Co co-substituted samples immersed in SBF; **(c)** concentration changes in Co; **(d)** concentration changes in Ca; **(e)** concentration changes in M; **(f)** concentration changes in Si; **(g)** P ions released from the Ce/Co co-substituted samples in SBF.

The cytotoxicity analysis results of the Ce/Co co-substituted samples are shown in Fig. 6(a). The Ce/Co co-substituted samples exhibited cytotoxicity, with cell viability progressively decreasing as the co-substitution level increased. The incorporation of Ce ions did not mitigate this response. Instead, the structural alterations induced by co-substitution reduced cell adhesion. These findings indicate that Co ion release is an important factor affecting the biocompatibility of the Ce/Co co-substituted samples. The mineralization of the Ce/Co co-substituted samples was adversely affected by the cytotoxicity of Co ions, resulting in suboptimal cell adhesion.

As shown in the OD value analysis in Fig. 6(b), elevated concentrations of both Ce and Co ions continued to exert noticeable effects on the samples. At higher co-substitution levels, Ce and Co ions suppressed the mineralization capability, indicating that excessive ion release hinders the osteogenic potential of the Ce/Co co-substituted samples. The different biological responses induced by Ce and Co co-substitution can be explained at the molecular level by their distinct interactions with cells and the local ionic environment. Ce^{3+}/Ce^{4+} ions exhibit redox activity that scavenges reactive oxygen species, reducing oxidative stress at the cell–material interface. This antioxidant effect, together with a more regulated ion-exchange behavior and stabilized local pH, improves cell adhesion and HPa formation at low Ce/Co substitution levels. In contrast, Co^{2+} ions induce cytotoxic effects through oxidative stress generation and interference with essential Ca^{2+}-and Mg^{2+}-dependent cellular processes. As the Co content increases, Co^{2+} ions release disrupts cellular homeostasis, reducing cell viability and mineralization. Therefore, while limited Ce/Co co-substitution enhances structural stability and surface bioactivity, excessive Co incorporation affects the biological response and results in compromised biocompatibility.

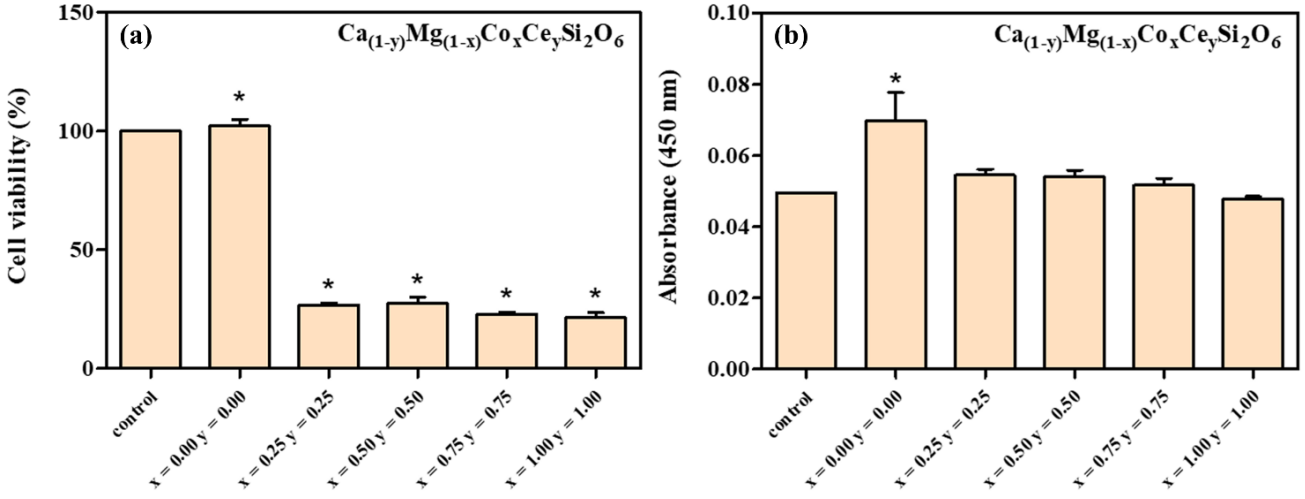

Fig. 6. **(a)** Cytotoxicity analysis; **(b)** ARS staining quantification of the Ce/Co co-substituted samples for 24 hours.

4. Conclusions

Co-substitution of Ce and Co ions into the diopside lattice was investigated for structural, mechanical, bioactive, and biological effects. The results indicate that low-to-moderate co-substitution (Ce 0.25–0.50 mol / Co 0.25–0.50 mol) provides the most favorable balance. Notably, the Ce 0.50 mol/ Co 0.50 mol composition exhibited the highest hardness (174.8 Hv), representing a >10-fold increase compared with pure diopside (14.9 Hv). Structural analysis results confirmed that low-to-moderate substitution preserved lattice stability, whereas higher levels (≥0.75/0.75 mol) induced distortion, increased porosity, and reduced mechanical strength. Bioactivity assessments revealed that Ce 0.25 mol/Co 0.25 mol promoted the most pronounced HAp deposition, consistent with reduced Ca and P depletion in SBF. In contrast, excessive substitution suppressed Si release and inhibited HAp nucleation. Degradation studies further showed that Ce 0.50 mol/ Co 0.50 mol had the slowest dissolution rate, while Ce 1.00 / Co 1.00 degraded rapidly.

Ion-release profiles demonstrated a proportional increase in Co release with substitution level, reducing biocompatibility. Cytotoxicity assay results showed a dose-dependent decline in cell viability, identifying Co ions as the primary factor impairing cellular response. High dopant concentrations also suppressed mineralization, as reflected by diminished ARS OD values. Overall, controlled Ce/Co co-substitution at low-to-moderate levels enhances structural densification and maintains acceptable mineralization capacity, whereas excessive incorporation compromises mechanical integrity, bioactivity, and cytocompatibility. The Ce 0.25–0.50 mol/Co 0.25–0.50 mol sample represents the optimal substitution window for developing diopside-based biomaterials. Within this range, Ce 0.25 mol/Co 0.25 mol sample shows the best balance of bioactivity and biocompatibility, while the Ce 0.50

mol/ Co 0.50 mol sample presents superior mechanical reinforcement. Therefore, Ce 0.25 mol/Co 0.25 mol is recommended for prioritizing osteogenic potential and cytocompatibility, whereas Ce 0.50 mol/Co 0.50 mol is preferable when mechanical strength is required. In further studies, Co levels to minimize cytotoxicity while preserving performance must be examined.

Author Contributions: These authors contributed equally to this work.

Funding: This research did not receive external funding.

Data Availability Statement: The data of this study are available from the corresponding author upon reasonable request.

Acknowledgments: The authors acknowledge financial support from the National Science and Technology Council under contract NSTC 114-2222-E-110-002 -MY2, the Field Emission Electron Probe Microanalyzer equipment provided by Joint Center for High Valued Instruments at National Sun Yat-Sen University, and the Inductively Coupled Plasma-Mass Spectrometer equipment provided by the Instrument Center of National Cheng Kung University, Taiwan. The authors thank National Center for High-performance Computing (NCHC) for providing computational and storage resources.

Conflicts of Interest: The authors declare no conflict of interest.

References

1. Padeiro, M.; Santana, P.; Grant, M. Chapter 1 - Global aging and health determinants in a changing world. In *Aging*; Oliveira, P.J., Malva, J.O., Eds.; Academic Press: Cambridge, MA, USA, 2023; pp. 3–30.
2. Yuan, Y.H.; Yuan, Q.J.; Wu, C.Z.; Ding, Z.F.; Wang, X.; Li, G.D.; Gu, Z.P.; Li, L.J.; Xie, H.X. Enhanced Osteoconductivity and Osseointegration in Calcium Polyphosphate Bioceramic Scaffold via Lithium Doping for Bone Regeneration. *ACS Biomater. Sci. Eng.* **2019**, *5*, 5872–5880.
3. Diefenbeck, M.; Mückley, T.; Schrader, C.; Schmidt, J.; Zankovych, S.; Bossert, J.; Jandt, K.D.; Faucon, M.; Finger, U. The effect of plasma chemical oxidation of titanium alloy on bone-implant contact in rats. *Biomaterials* **2011**, *32*, 8041–8047.
4. Magnan, B.; Bondi, M.; Maluta, T.; Samaila, E.; Schirru, L.; Dall'Oca, C. Acrylic bone cement: current concept review. *Musculoskelet. Surg.* **2013**, *97*, 93–100. https://doi.org/10.1007/s12306-013-0293-9
5. Crawford, C.H., III; Carreon, L.Y.; McGinnis, M.D.; Campbell, M.J.; Glassman, S.D. Perioperative complications of recombinant human bone morphogenetic protein-2 on an absorbable collagen sponge versus iliac crest bone graft for posterior cervical arthrodesis. *Spine* **2009**, *34*, 1390–1394.
6. Bose, S.; Fielding, G.; Tarafder, S.; Bandyopadhyay, A. Understanding of dopant-induced osteogenesis and angiogenesis in calcium phosphate ceramics. *Trends Biotechnol.* **2013**, *31*, 594–605. https://doi.org/10.1016/j.tibtech.2013.06.005
7. Wong, H.M.; Yeung, K.W.; Lam, K.O.; Tam, V.; Chu, P.K.; Luk, K.D.; Cheung, K.M. A biodegradable polymer-based coating to control the performance of magnesium alloy orthopaedic implants. *Biomaterials* **2010**, *31*, 2084–2096. https://doi.org/10.1016/j.biomaterials.2009.11.111
8. Yoshizawa, S.; Brown, A.; Barchowsky, A.; Sfeir, C. Role of magnesium ions on osteogenic response in bone marrow stromal cells. *Connect. Tissue Res.* **2014**, *55* (Suppl. 1), 155–159.
9. Yoshizawa, S.; Brown, A.; Barchowsky, A.; Sfeir, C. Magnesium ion stimulation of bone marrow stromal cells enhances osteogenic activity, simulating the effect of magnesium alloy degradation. *Acta Biomater.* **2014**, *10*, 2834–2842. https://doi.org/10.1016/j.actbio.2014.02.002
10. Verberckmoes, S.C.; De Broe, M.E.; D'Haese, P.C. Dose-dependent effects of strontium on osteoblast function and mineralization. *Kidney Int.* **2003**, *64*, 534–543. https://doi.org/10.1046/j.1523-1755.2003.00123.x
11. Li, Y.; Li, J.; Zhu, S.; Luo, E.; Feng, G.; Chen, Q.; Hu, J. Effects of strontium on proliferation and differentiation of rat bone marrow mesenchymal stem cells. *Biochem. Biophys. Res. Commun.* **2012**, *418*, 725–730.
12. Reffitt, D.; Ogston, N.; Jugdaohsingh, R.; Cheung, H.; Evans, B.A.J.; Thompson, R.; Powell, J.; Hampson, G. Orthosilicic acid stimulates collagen type 1 synthesis and osteoblastic differentiation in human osteoblast-like cells in vitro. *Bone* **2003**, *32*, 127–135.
13. Gaharwar, A.K.; Mihaila, S.M.; Swami, A.; Patel, A.; Sant, S.; Reis, R.L.; Marques, A.P.; Gomes, M.E.; Khademhosseini, A. Bioactive silicate nanoplatelets for osteogenic differentiation of human mesenchymal stem cells. *Adv. Mater.* **2013**, *25*, 3329–3336. https://doi.org/10.1002/adma.201300584
14. Yamaguchi, M.; Goto, M.; Uchiyama, S.; Nakagawa, T. Effect of zinc on gene expression in osteoblastic MC3T3-E1 cells: enhancement of Runx2, OPG, and regucalcin mRNA expressions. *Mol. Cell. Biochem.* **2008**, *312*, 157–166.
15. Kwun, I.-S.; Cho, Y.-E.; Lomeda, R.-A.R.; Shin, H.-I.; Choi, J.-Y.; Kang, Y.-H.; Beattie, J.H. Zinc deficiency suppresses matrix mineralization and retards osteogenesis transiently with catch-up possibly through Runx 2 modulation. *Bone* **2010**, *46*, 732–741.
16. Popp, J.R.; Love, B.J.; Goldstein, A.S. Effect of soluble zinc on differentiation of osteoprogenitor cells. *J. Biomed. Mater. Res. Part A* **2007**, *81*, 766–769.

17. Chen, Y.; Whetstone, H.C.; Lin, A.C.; Nadesan, P.; Wei, Q.; Poon, R.; Alman, B.A. Beta-catenin signaling plays a disparate role in different phases of fracture repair: implications for therapy to improve bone healing. *PLoS Med.* **2007**, *4*, e249. https://doi.org/10.1371/journal.pmed.0040249
18. Fan, W.; Crawford, R.; Xiao, Y. Enhancing in vivo vascularized bone formation by cobalt chloride-treated bone marrow stromal cells in a tissue engineered periosteum model. *Biomaterials* **2010**, *31*, 3580–3589.
19. Wu, C.; Zhou, Y.; Fan, W.; Han, P.; Chang, J.; Yuen, J.; Zhang, M.; Xiao, Y. Hypoxia-mimicking mesoporous bioactive glass scaffolds with controllable cobalt ion release for bone tissue engineering. *Biomaterials* **2012**, *33*, 2076–2085. https://doi.org/10.1016/j.biomaterials.2011.11.042
20. Quinlan, E.; Partap, S.; Azevedo, M.M.; Jell, G.; Stevens, M.M.; O'Brien, F.J. Hypoxia-mimicking bioactive glass/collagen glycosaminoglycan composite scaffolds to enhance angiogenesis and bone repair. *Biomaterials* **2015**, *52*, 358–366. https://doi.org/10.1016/j.biomaterials.2015.02.006
21. Shalumon, K.; Sowmya, S.; Sathish, D.; Chennazhi, K.; Nair, S.V.; Jayakumar, R. Effect of incorporation of nanoscale bioactive glass and hydroxyapatite in PCL/chitosan nanofibers for bone and periodontal tissue engineering. *J. Biomed. Nanotechnol.* **2013**, *9*, 430–440.
22. Demina, V.A.; Krasheninnikov, S.V.; Buzin, A.I.; Kamyshinsky, R.A.; Sadovskaya, N.V.; Goncharov, E.N.; Zhukova, N.A.; Khvostov, M.V.; Pavlova, A.V.; Tolstikova, T.G. Biodegradable poly (l-lactide)/calcium phosphate composites with improved properties for orthopedics: effect of filler and polymer crystallinity. *Mater. Sci. Eng. C* **2020**, *112*, 110813. https://doi.org/10.1016/j.msec.2020.110813
23. Zhao, J.; Lu, X.; Duan, K.; Guo, L.; Zhou, S.; Weng, J. Improving mechanical and biological properties of macroporous HA scaffolds through composite coatings. *Colloids Surf. B Biointerfaces* **2009**, *74*, 159–166.
24. Jacobs, A.; Renaudin, G.; Forestier, C.; Nedelec, J.-M.; Descamps, S. Biological properties of copper-doped biomaterials for orthopedic applications: A review of antibacterial, angiogenic and osteogenic aspects. *Acta Biomater.* **2020**, *117*, 21–39. https://doi.org/10.1016/j.actbio.2020.09.044
25. Uysal, I.; Severcan, F.; Tezcaner, A.; Evis, Z. Co-doping of hydroxyapatite with zinc and fluoride improves mechanical and biological properties of hydroxyapatite. *Prog. Nat. Sci. Mater. Int.* **2014**, *24*, 340–349.
26. Boanini, E.; Gazzano, M.; Bigi, A. Ionic substitutions in calcium phosphates synthesized at low temperature. *Acta Biomater.* **2010**, *6*, 1882–1894. https://doi.org/10.1016/j.actbio.2009.12.041
27. Gomes, S.; Vichery, C.; Descamps, S.; Martinez, H.; Kaur, A.; Jacobs, A.; Nedelec, J.-M.; Renaudin, G. Cu-doping of calcium phosphate bioceramics: From mechanism to the control of cytotoxicity. *Acta Biomater.* **2018**, *65*, 462–474. https://doi.org/10.1016/j.actbio.2017.10.028
28. Kaur, P.; Singh, K.; Yadav, A.K.; Kaur, S.; Kaur, R.; Kaur, S. Growth of bone like hydroxyapatite and cell viability studies on CeO2 doped CaO–P2O5–MgO–SiO2 bioceramics. *Mater. Chem. Phys.* **2020**, *243*, 122352. https://doi.org/10.1016/j.matchemphys.2019.122352
29. Sobhanachalam, P.; Kumar, V.R.; Venkatramaiah, N.; Gandhi, Y.; Veeraiah, N. Synthesis and in vitro characterization of cerium oxide mixed calcium oxy fluoro borophosphate bioactive glasses by means of spectroscopic studies. *J. Non-Cryst. Solids* **2018**, *498*, 422–429.
30. Shannon, R.D. Revised effective ionic radii and systematic studies of interatomic distances in halides and chalcogenides. *Acta Crystallogr. Sect. A* **1976**, *32*, 751–767.
31. Kilbourn, B.T. Cerium and cerium compounds. In *Kirk-Othmer Encyclopedia of Chemical Technology*; John Wiley & Sons, Inc.: Hoboken, NJ, USA, 2000; pp. 1–23. https://doi.org/10.1002/0471238961.0305180911091202.a01
32. Rad, R.M.; Alshemary, A.Z.; Evis, Z.; Keskin, D.; Tezcaner, A. Cellulose acetate-gelatin-coated boron-bioactive glass biocomposite scaffolds for bone tissue engineering. *Biomed. Mater.* **2020**, *15*, 065009.
33. Sahu, T.; Singh Bisht, S.; Ranjan Das, K.; Kerkar, S. Nanoceria: synthesis and biomedical applications. *Curr. Nanosci.* **2013**, *9*, 588–593.
34. 7Hu, Y.; Du, Y.; Jiang, H.; Jiang, G.-S. Cerium promotes bone marrow stromal cells migration and osteogenic differentiation via Smad1/5/8 signaling pathway. *Int. J. Clin. Exp. Pathol.* **2014**, *7*, 5369–5378.
35. Jakupec, M.A.; Unfried, P.; Keppler, B.K. Pharmacological properties of cerium compounds. *Rev. Physiol. Biochem. Pharmacol.* **2005**, *153*, 101–111.
36. Malda, J.; Klein, T.J.; Upton, Z. The roles of hypoxia in the in vitro engineering of tissues. *Tissue Eng.* **2007**, *13*, 2153–2162. https://doi.org/10.1089/ten.2006.0417
37. Tian, T.; Han, Y.; Ma, B.; Wu, C.; Chang, J. Novel Co-akermanite (Ca2CoSi2O7) bioceramics with the activity to stimulate osteogenesis and angiogenesis. *J. Mater. Chem. B* **2015**, *3*, 6773–6782.
38. Si, W.; Li, S. Crystallization kinetics of diopside glass ceramics. *J. Phys. Conf. Ser.* **2020**, *1549*, 032128.
39. Eoh, Y.J.; Kim, E.S. Effect of heat-treatment on the dielectric properties of CaMgSi2O6 glass-ceramics with Cr2O3–Fe2O3–TiO2. *Jpn. J. Appl. Phys.* **2014**, *53*, 08NB01. https://doi.org/10.7567/JJAP.53.08NB01
40. Kokubo, T.; Takadama, H. How useful is SBF in predicting in vivo bone bioactivity? *Biomaterials* **2006**, *27*, 2907–2915. https://doi.org/10.1016/j.biomaterials.2006.01.017

41. Ansari, A.A.; Labis, J.; Alam, M.; Ramay, S.M.; Ahmad, N.; Mahmood, A. Effect of cobalt doping on structural, optical and redox properties cerium oxide nanoparticles. *Phase Transit.* **2016**, *89*, 261–272.
42. Khadar, Y.S.; Balamurugan, A.; Devarajan, V.; Subramanian, R.; Kumar, S.D. Synthesis, characterization and antibacterial activity of cobalt doped cerium oxide (CeO2: Co) nanoparticles by using hydrothermal method. *J. Mater. Res. Technol.* **2019**, *8*, 267–274.
43. Ranjith, K.S.; Saravanan, P.; Chen, S.-H.; Dong, C.-L.; Chen, C.L.; Chen, S.-Y.; Asokan, K.; Rajendra Kumar, R.T. Enhanced room-temperature ferromagnetism on Co-doped CeO2 nanoparticles: mechanism and electronic and optical properties. *J. Phys. Chem. C* **2014**, *118*, 27039–27047.
44. Rochard, G.; Giraudon, J.-M.; Liotta, L.F.; La Parola, V.; Lamonier, J.-F. Au/Co promoted CeO2 catalysts for formaldehyde total oxidation at ambient temperature: role of oxygen vacancies. *Catal. Sci. Technol.* **2019**, *9*, 3203–3213.